

# Big to Small: Ultrafine Mo<sub>2</sub>C Particles Derived from Giant Polyoxomolybdate Clusters for Hydrogen Evolution Reaction

Zheng Zhou, Ziwen Yuan, Sai Li, Hao Li, Junsheng Chen, Yanqing Wang, Qianwei Huang, Cheng Wang, Huseyin Enis Karahan, Graeme Henkelman, Xiaozhou Liao, Li Wei,\* and Yuan Chen\*

Due to its electronic structure, similar to platinum, molybdenum carbides (Mo<sub>2</sub>C) hold great promise as a cost-effective catalyst platform. However, the realization of high-performance Mo<sub>2</sub>C catalysts is still limited because controlling their particle size and catalytic activity is challenging with current synthesis methods. Here, the synthesis of ultrafine  $\beta$ -Mo<sub>2</sub>C nanoparticles with narrow size distribution ( $2.5 \pm 0.7$  nm) and high mass loading (up to 27.5 wt%) on graphene substrate using a giant Mo-based polyoxomolybdate cluster, Mo<sub>132</sub> ((NH<sub>4</sub>)<sub>42</sub>[Mo<sub>132</sub>O<sub>372</sub>(CH<sub>3</sub>COO)<sub>30</sub>(H<sub>2</sub>O)<sub>72</sub>] $\cdot$ 10CH<sub>3</sub>COONH<sub>4</sub> $\cdot$ 300H<sub>2</sub>O) is demonstrated. Moreover, a nitrogen-containing polymeric binder (polyethylenimine) is used to create Mo–N bonds between Mo<sub>2</sub>C nanoparticles and nitrogen-doped graphene layers, which significantly enhance the catalytic activity of Mo<sub>2</sub>C for the hydrogen evolution reaction, as is revealed by X-ray photoelectron spectroscopy and density functional theory calculations. The optimal Mo<sub>2</sub>C catalyst shows a large exchange current density of 1.19 mA cm<sup>-2</sup>, a high turnover frequency of 0.70 s<sup>-1</sup> as well as excellent durability. The demonstrated new strategy opens up the possibility of developing practical platinum substitutes based on Mo<sub>2</sub>C for various catalytic applications.

large scale.<sup>[2]</sup> Among the potential material candidates, molybdenum carbides (Mo<sub>x</sub>C) have attracted substantial interests.<sup>[3]</sup> The d-band electronic structure of Mo<sub>x</sub>C materials is similar to Pt, resulting in good electrical conductivity and optimal H intermediate adsorption energies.<sup>[4]</sup> Particularly, the  $\beta$ -Mo<sub>2</sub>C phase exhibits higher catalytic activity for HER in both acidic and basic electrolytes among different phases of Mo<sub>x</sub>C.<sup>[5]</sup> But still, their catalytic performance is insufficient for practical HER applications.

Recent efforts for improving Mo<sub>x</sub>C catalysts (MoC and Mo<sub>2</sub>C) focus on three general design strategies.<sup>[1d,3a]</sup> One strategy is to increase the density of active catalytic sites by depositing a large amount of Mo<sub>x</sub>C nanoparticles on substrates with a large specific surface area. Carbon nanotubes, graphene materials, and conductive polymeric materials (e.g., polypyrrole or polyaniline)<sup>[4a,6]</sup> are among the tested

Electrochemical water splitting using electricity produced from renewable energy sources is a promising method for producing hydrogen (H<sub>2</sub>) as a sustainable fuel.<sup>[1]</sup> However, efficient electrocatalysts for hydrogen evolution reaction (HER) are often based on rare and costly platinum (Pt)-based materials. Therefore, developing electrocatalysts based on earth-abundant materials is important to economically produce H<sub>2</sub> at

candidates as substrates. Another strategy is to generate Mo<sub>x</sub>C nanostructures with a large specific surface area themselves using various templates, such as metal–organic frameworks and SiO<sub>2</sub> nanoparticles.<sup>[6a,7]</sup> The third direction is to enhance the intrinsic catalytic activity of Mo<sub>x</sub>C by forming strong couplings with catalyst substrates, such as N-doped carbon materials, creating defect sites, or doping different elements in

Z. Zhou, Z. Yuan, J. Chen, C. Wang, Dr. L. Wei, Prof. Y. Chen  
School of Chemical and Biomolecular Engineering  
The University of Sydney  
Sydney, New South Wales 2006, Australia  
E-mail: l.wei@sydney.edu.au; yuan.chen@sydney.edu.au

Prof. S. Li  
School of Chemical Engineering  
Sichuan University  
Chengdu, Sichuan 610065, China

H. Li, Prof. G. Henkelman  
Department of Chemistry and the Institute for Computational  
and Engineering Sciences  
The University of Texas at Austin  
105 E. 24th Street, Stop A5300, Austin, TX 78712, USA

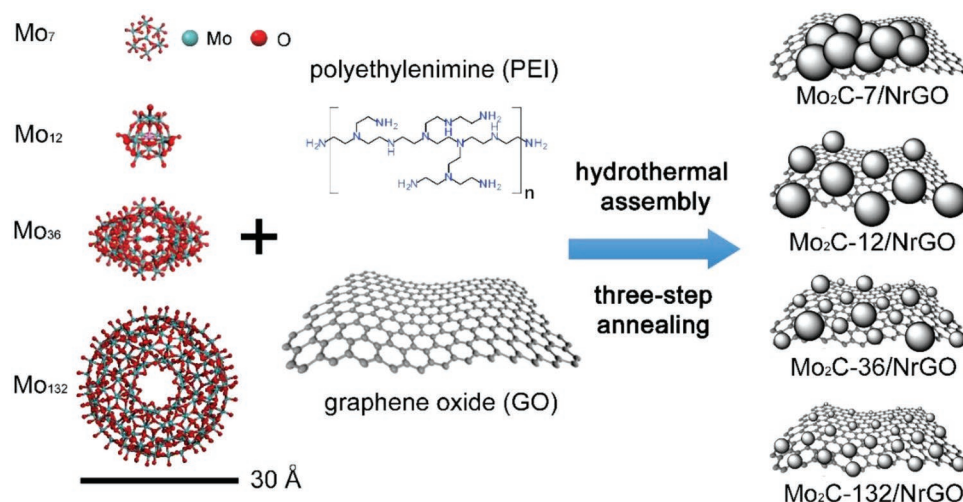
Dr. Y. Wang  
Faculty of Engineering  
The University of Tokyo  
Yayoi, Bunkyo-Ku, Tokyo 113-00, Japan

Q. Huang, Prof. X. Liao  
School of Aerospace  
Mechanical and Mechatronic Engineering  
The University of Sydney  
Sydney, New South Wales 2006, Australia

Dr. H. E. Karahan  
School of Chemical and Biomedical Engineering  
Nanyang Technological University  
Singapore 637459, Singapore

 The ORCID identification number(s) for the author(s) of this article can be found under <https://doi.org/10.1002/sml.201900358>.

DOI: 10.1002/sml.201900358



**Scheme 1.** Schematic illustration of the synthesis of Mo<sub>2</sub>C- $\gamma$ /NrGO- $z$  catalysts.

Mo <sub>$x$</sub> C.<sup>[3b,8]</sup> These approaches are often combined to benefit from synergistic effects.<sup>[3a]</sup>

The synthesis of Mo <sub>$x$</sub> C inevitably involves high-temperature thermal treatment (typically >800 °C), which often leads to poor control over size distribution of Mo <sub>$x$</sub> C particles.<sup>[9]</sup> An essential aspect of the synthesis of Mo <sub>$x$</sub> C catalysts is the selection of a suitable Mo precursor. The commonly used Mo precursors include molybdenum salts (e.g., MoCl<sub>5</sub>), monomolybdates (e.g., Na<sub>2</sub>MoO<sub>4</sub> or (NH<sub>4</sub>)<sub>2</sub>MoO<sub>4</sub>), and small-sized polyoxomolybdates (POMs), such as (NH<sub>4</sub>)<sub>2</sub>Mo<sub>4</sub>O<sub>13</sub> (denoted as Mo<sub>4</sub>), (NH<sub>4</sub>)<sub>6</sub>Mo<sub>7</sub>O<sub>24</sub>·4H<sub>2</sub>O (denoted as Mo<sub>7</sub>), and H<sub>3</sub>PMo<sub>12</sub>O<sub>40</sub>· $n$ H<sub>2</sub>O (denoted as Mo<sub>12</sub>).<sup>[4b,6b,c,8a,b,d,e,10]</sup> During high-temperature thermal treatments, Mo particles derived from those small precursors are likely to grow into large particles with a broad size distribution. In fact, all existing methods have difficulty in increasing the Mo mass loading higher than 20 wt% without seeing significant coalescence of Mo <sub>$x$</sub> C.<sup>[11]</sup> In this context, we hypothesized that employing a giant POM with a size similar to that of the targeted Mo <sub>$x$</sub> C nanoparticles should create uniform nano-Mo <sub>$x$</sub> C catalysts. Further, we proposed that preanchoring the giant POM clusters on graphene using a polymeric binder, would enable the uniform distribution and suppress the mobility and hence coalescence of Mo <sub>$x$</sub> C particles during chemical transformation.

Here, we describe the synthesis of highly uniform ultrafine Mo<sub>2</sub>C nanoparticles anchored on graphene-based substrates starting with a giant POM constituted of 132 Mo atoms per cluster (Mo<sub>132</sub>). We found that smaller POMs, including Mo<sub>7</sub>, Mo<sub>12</sub>, and K<sub>8</sub>[Mo<sub>36</sub>O<sub>112</sub>(H<sub>2</sub>O)<sub>16</sub>]·36H<sub>2</sub>O (Mo<sub>36</sub>), provide poor control over the size distribution of Mo<sub>2</sub>C nanoparticles when the mass loadings of Mo are increased. In contrast, the giant POM enables the formation of Mo<sub>2</sub>C nanoparticles with a narrow size distribution range (2.5 ± 0.7 nm) even at a high mass loading. Furthermore, based on X-ray photoelectron spectroscopy (XPS) measurements, we observed the formation of strong Mo–N bonds between the Mo<sub>2</sub>C nanoparticles and the N-doped and reduced graphene oxide (NrGO) substrate due primarily to the polymeric binder used (polyethyleneimine, PEI). The strong chemical coupling provides a low overpotential, large exchange

current density, and a high turnover frequency for HER. Importantly, density functional theory (DFT) calculations verify the crucial role of catalyst–substrate coupling for improving HER activity. Our results demonstrate the benefit of using a giant POM as well as a polymeric binder for tailoring the catalytic properties of Mo<sub>2</sub>C-based catalysts. As a general approach, the giant POM-based synthesis of metal carbide nanoparticles holds great promise for designing high-performance catalysts.

The synthesis of Mo<sub>2</sub>C catalysts comprised of Mo<sub>2</sub>C nanoparticles anchored on NrGO is illustrated in **Scheme 1**. They are denoted as Mo<sub>2</sub>C- $\gamma$ /NrGO- $z$ , where  $\gamma$  refers to the number of Mo atoms in Mo precursors, and  $z$  refers to the mass loading of Mo in hybrid materials. Four types of Mo precursors in different sizes ranging from 8 to 27 Å (i.e., 8, 12, 19, 27 Å) were used, including Mo<sub>7</sub>, Mo<sub>12</sub>, Mo<sub>36</sub>, and Mo<sub>132</sub>. Mo<sub>7</sub> and Mo<sub>12</sub> are commercially available. Mo<sub>36</sub> and Mo<sub>132</sub> precursors were synthesized according to the methods in previous reports as described in the Experimental Section.<sup>[12]</sup> The successful synthesis was confirmed by Fourier transform infrared (FTIR) spectroscopy measurement presented in Figure S1 (Supporting Information).<sup>[12b,c]</sup> Different amounts of Mo <sub>$\gamma$</sub>  precursors in aqueous solutions were first mixed with an aqueous suspension of PEI-coated GO under vigorous stirring. PEI was used here for the following considerations: (1) the positively charged PEI assists the binding between Mo precursors and negatively charged GO; (2) PEI serves as a carbon precursor for Mo<sub>2</sub>C nanocluster formation, which minimizes the etching of GO by MoO <sub>$x$</sub>  during the high-temperature annealing;<sup>[8b]</sup> (3) PEI provides abundant N atoms to dope GO and assist the formation of Mo–N bonds. The amount of added PEI was also optimized because it can affect the content of N, thus affecting HER performance. The GO:PEI mass ratio of 2:1 (corresponding to 20 mg of PEI used in one synthesis) was found to be the optimal condition. Further increasing the PEI amount leads to severe GO flocculation and nonuniform distribution of Mo<sub>2</sub>C particles (see Figure S2, Supporting Information). The mixture of Mo <sub>$\gamma$</sub>  precursor and PEI-GO then underwent hydrothermal reaction, resulting in the precipitation of solid materials. After freeze-drying, the solid materials were treated by a three-step

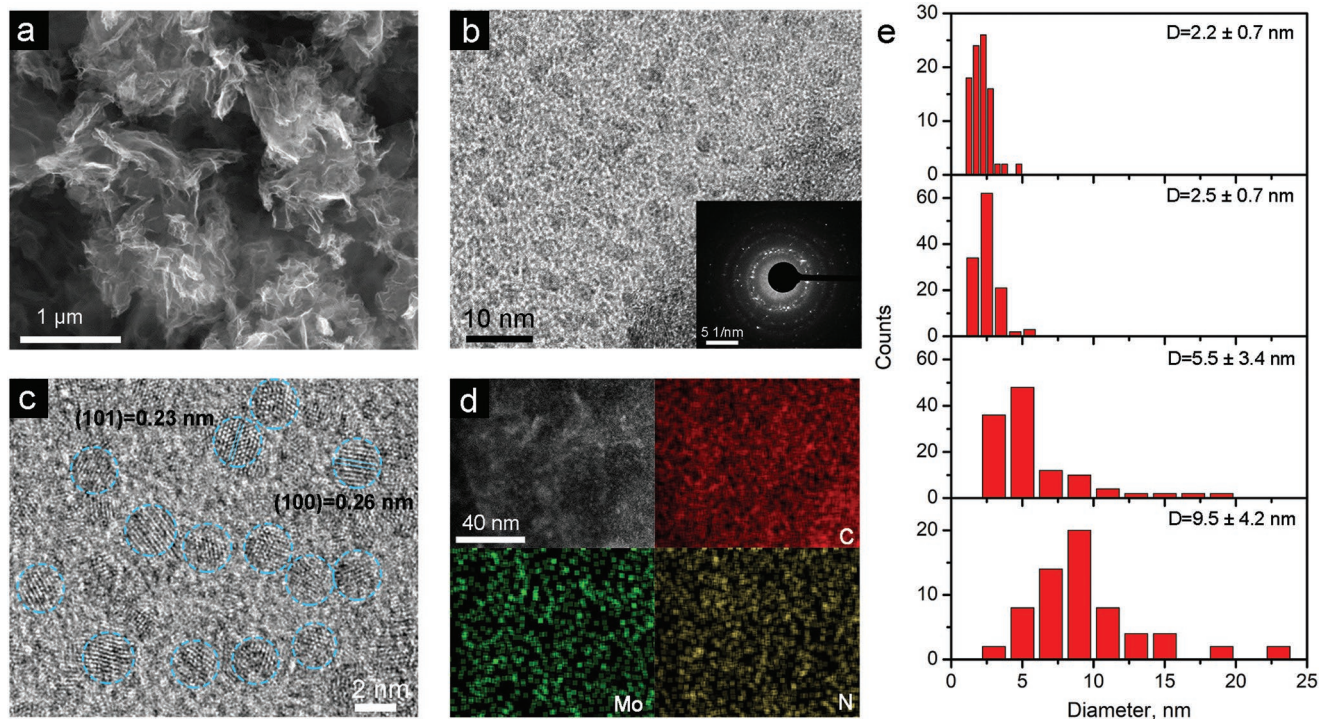


**Figure 1.** Characterization of Mo<sub>2</sub>C-132/NrGO-30 catalysts. a) SEM image. b,c) TEM images at different magnifications. The inset of (b) shows the corresponding SAED pattern. d) HAADF-STEM and the corresponding EDX mapping results. e) Size distributions of Mo<sub>2</sub>C nanoparticles in Mo<sub>2</sub>C-132/NrGO-z obtained by TEM analysis. From top to bottom, z is at 15, 30, 45, and 60, respectively.

annealing process. They were first heated and annealed at 300 °C in air to convert POMs to Mo oxides, followed by reduction in H<sub>2</sub> at 300 °C for 30 min to prevent the formation of volatile MoO<sub>3</sub>, which would evaporate above 700 °C before or during the formation of Mo<sub>2</sub>C and result in the loss of Mo.<sup>[13]</sup> The final annealing temperature was further optimized, and 850 °C was found to be the optimal condition (see Figures S3–S5 and the related discussion in the Supporting Information). The reduced materials were heated to 850 °C in Ar and kept at that temperature for 2 h to form Mo<sub>2</sub>C-γ/NrGO-z catalysts.

We first explored the effect of loading different amounts of Mo<sub>132</sub> precursors on the morphology of resulting nano-Mo<sub>2</sub>C particles. It is desirable to have high Mo mass loadings while retaining ultrafine particles so that Mo<sub>2</sub>C catalysts have a high density of active catalytic sites. By adding different amounts of Mo<sub>132</sub> precursors in the mixture of Mo precursor and PEI-GO, four Mo<sub>2</sub>C-132/NrGO-z with Mo mass loadings ranging from 15 to 60 wt% were prepared. As shown in **Figure 1a** and **Figure S6** (Supporting Information), no large aggregates of Mo<sub>2</sub>C particles are observed with scanning electron microscope (SEM). Elemental mappings carried out by energy-dispersive X-ray spectroscopy (EDS) show that C, N, O, and Mo all distribute uniformly in Mo<sub>2</sub>C-132/NrGO-z (**Figure S6**, Supporting Information). The mass loading of Mo in Mo<sub>2</sub>C-132/NrGO-z was measured by EDS, XPS, and inductively coupled plasma atomic emission spectroscopy (ICP-AES). As shown in **Table S1** (Supporting Information), the Mo content in Mo<sub>2</sub>C-132/NrGO-z correlates with the initially added Mo mass fractions. For example, there is 26.2 wt% (EDS) of Mo in Mo<sub>2</sub>C-132/NrGO-30 versus 30 wt% added, suggesting insignificant Mo

loss in the synthesis. The value determined by EDS is also consistent with those determined by XPS (29.3 wt%) and ICP-AES (27.5 wt%). Considering XPS and EDS are more surface-sensitive techniques while ICP-AES provides the elemental concentration in the bulk, these results suggest a uniform elemental distribution of Mo in Mo<sub>2</sub>C-132/NrGO-z. Additionally, the SEM image of Mo<sub>2</sub>C-132/NrGO-30 shown in **Figure 1a** displayed a laminated and wrinkled graphene structure. Analysis of its N<sub>2</sub> physisorption isotherms in **Figure S7** (Supporting Information) indicates that it has a large Brunauer–Emmett–Teller (BET) specific surface area of 251.2 m<sup>2</sup> g<sup>-1</sup> and abundant mesopores with an average pore diameter of 5 nm. The large surface area and pore structure are beneficial to expose more active catalyst surface and facilitate mass transfer.

High-resolution transmission electron microscope (TEM) was used to characterize Mo<sub>2</sub>C nanoclusters in Mo<sub>2</sub>C-132/NrGO-z. As shown in **Figure 1b** (Mo<sub>2</sub>C-132/NrGO-30) and **Figure S8** (Supporting Information) (Mo<sub>2</sub>C-132/NrGO-15, -45, and -60), Mo<sub>2</sub>C nanoparticles distribute uniformly on graphene surface with no apparent aggregation, which is favorable for exposing more catalytically active sites. The inset of **Figure 1b** shows well-defined diffraction rings obtained by selected area electron diffraction (SAED), which can be assigned to various crystalline facets of β-Mo<sub>2</sub>C. The corresponding lattice fringes are identified with TEM observation as shown in **Figure 1c**. β-Mo<sub>2</sub>C is desirable for Mo<sub>2</sub>C-based HER catalysts because it has the highest activity among all Mo<sub>2</sub>C phases.<sup>[5]</sup> The formation of β-Mo<sub>2</sub>C in Mo<sub>2</sub>C-132/NrGO-z is further confirmed by powder X-ray diffraction (PXRD, see **Figure S9**, Supporting Information), in which no diffraction peaks from other Mo<sub>2</sub>C

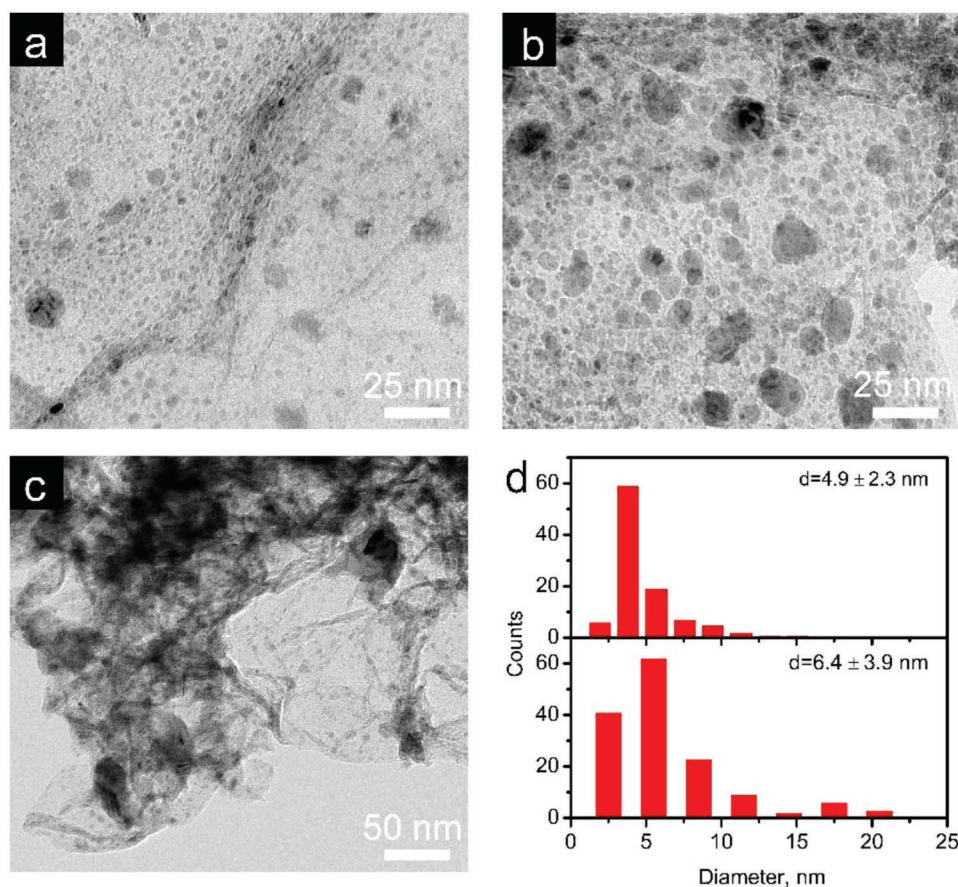


**Figure 2.** a–c) TEM images of Mo<sub>2</sub>C- $\gamma$ /NrGO-30 electrocatalysts prepared using Mo<sub>36</sub>, Mo<sub>12</sub>, and Mo<sub>7</sub> precursors. d) Particle size distributions of Mo<sub>2</sub>C nanoclusters in Mo<sub>2</sub>C-36/NrGO-30 (top) and Mo<sub>2</sub>C-12/NrGO-30 (bottom) determined by TEM.

phases are observed. Figure 1d shows a high-resolution scanning transmission electron microscope (STEM) image of the electrocatalyst obtained under the high-angle annular dark-field (HAADF) mode together with its corresponding EDX elemental mapping results, which further confirmed the formation of numerous ultrafine Mo<sub>2</sub>C nanoparticles on the N-doped graphene nanosheets. TEM images show that the size of Mo<sub>2</sub>C nanoclusters grows larger with the increase of Mo mass loading. About 100–120 nanoclusters were measured for each sample to determine their size distribution. As shown in Figure 1e, Mo<sub>2</sub>C nanoclusters in Mo<sub>2</sub>C-132/NrGO-15 have an average size of  $2.2 \pm 0.7$  nm, which is similar to those in Mo<sub>2</sub>C-132/NrGO-30 at  $2.5 \pm 0.7$  nm even though the Mo mass loading is doubled. It is notable that the observed particle size (2.5 nm) is close to the theoretical size of a Mo<sub>2</sub>C particle formed from a single Mo<sub>132</sub> cluster of 1.7 nm (by using a  $V_{\text{cell}} = 37.2 \text{ \AA}^3$  (PDF No. 35-0787) and assuming the formation of a spherical particle), which suggests a nearly “one Mo<sub>132</sub> cluster” to “one Mo<sub>2</sub>C nanoparticle” conversion in the electrocatalyst preparation, which has not been reported before. However, when the Mo loadings increase to 45 and 60 wt%, the nanocluster sizes increase significantly to  $5.5 \pm 3.4$  and  $9.5 \pm 4.2$  nm, respectively. The standard deviations of their average particle size are also much larger, indicating the formation of particle aggregates. Based on these results, we conclude that the 30 wt% Mo mass loading is the

optimal condition for obtaining Mo<sub>2</sub>C-132/NrGO-*z* with uniform Mo<sub>2</sub>C nanoparticles. This Mo mass loading is also used in the following studies for testing the remaining experimental parameters.

Next, we study the role of using Mo precursors with different sizes. PXRD results in Figure S9 (Supporting Information) indicate the formation of  $\beta$ -Mo<sub>2</sub>C in these catalysts. However, SEM images and the corresponding EDX elemental mappings in Figures S10–S12 (Supporting Information) show that the Mo elemental distribution of Mo is nonuniform when smaller Mo precursors are used at the Mo mass loading of 30 wt%. For example, Mo<sub>2</sub>C-7/NrGO-30 shows significant segregation of Mo (Figure S10c, Supporting Information). The TEM images in Figure 2 also clearly show large Mo<sub>2</sub>C aggregates. The corresponding average size of Mo<sub>2</sub>C nanoparticles in Mo<sub>2</sub>C-36/NrGO-30 and Mo<sub>2</sub>C-12/NrGO-30 (Figure 2d) is  $4.9 \pm 2.3$  and  $6.4 \pm 3.9$  nm, respectively, which is 2–3 times larger than that of Mo<sub>2</sub>C nanoparticles in Mo<sub>2</sub>C-132/NrGO-30 (Figure 1e). It is difficult to perform a reliable size distribution analysis of Mo<sub>2</sub>C particles in Mo<sub>2</sub>C-7/NrGO-30 because of their severe aggregation. The results demonstrate the unique advantage of using the giant Mo<sub>132</sub> precursor in obtaining Mo<sub>2</sub>C nanoparticles with uniform size distribution and high mass loading on graphene substrates. We propose that this advantage can be attributed to two factors that influence the aggregation of nanoparticles

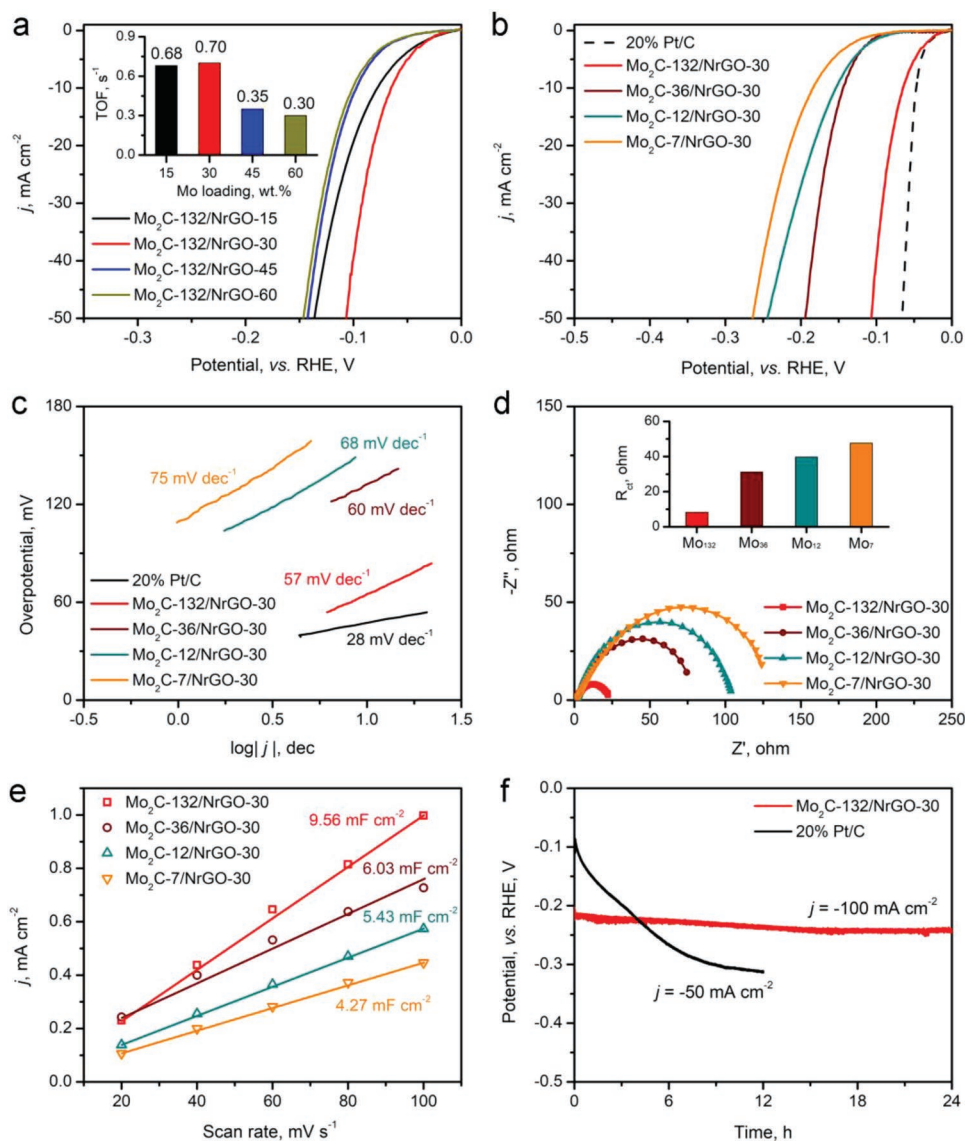


**Figure 3.** HER performance of  $\text{Mo}_2\text{C-}\gamma/\text{NrGO-}z$  and reference catalysts in  $0.5 \text{ M H}_2\text{SO}_4$  electrolyte. a) LSV curves of  $\text{Mo}_2\text{C-132/NrGO-}z$  catalysts, and the inset shows their calculated TOFs at  $\eta = 100 \text{ mV}$ . b) LSV, c) Tafel plots, and d) EIS Nyquist plots of  $\text{Mo}_2\text{C-}\gamma/\text{NrGO-}30$  and the reference catalysts. The inset in (d) compares their  $R_{\text{ct}}$  values. e)  $C_{\text{dl}}$  values of these catalysts. f) Stability test of the optimized  $\text{Mo}_2\text{C-132/NrGO-30}$  catalyst.

during the high-temperature treatment required for  $\text{Mo}_2\text{C}$  synthesis. (1) Since  $\text{Mo}_{132}$  clusters have much larger size, at the same Mo mass loading, the average interparticle distance among  $\text{Mo}_{132}$  clusters is much larger compared to the smaller Mo clusters. Based on a few simple assumptions, the average interparticle distance among  $\text{Mo}_{132}$  clusters is 4.3 times the distance among  $\text{Mo}_7$  clusters as discussed in the Supporting Information. (2) Larger  $\text{Mo}_{132}$  clusters would have better contact with the graphene substrates and may form stronger interactions, resulting in lower mobility compared to their smaller counterparts.

The HER performance of the  $\text{Mo}_2\text{C-}\gamma/\text{NrGO-}z$  catalyst was assessed on a glassy carbon electrode (GCE) in  $0.5 \text{ M H}_2\text{SO}_4$  electrolyte saturated with  $\text{H}_2$  using the standard three-electrode configuration as described in the Experimental Section. All reported potentials were calibrated to a reversible hydrogen electrode

(RHE). We first compared the performance of  $\text{Mo}_2\text{C-132/NrGO-}z$  catalysts synthesized using  $\text{Mo}_{132}$  precursors with different Mo mass loadings. **Figure 3a** and **Table 1** show that  $\text{Mo}_2\text{C-132/NrGO-30}$  exhibits the best HER performance among the four  $\text{Mo}_2\text{C-132/NrGO-}z$  catalysts. A small overpotential ( $\eta_{10}$ ) of 62 mV is required to deliver a current density ( $j$ ) of  $10 \text{ mA cm}^{-2}$ , which is smaller than the  $\eta_{10}$  of 73, 94 and 100 mV required for  $\text{Mo}_2\text{C-132/NrGO-15}$ , -45, and -60, respectively. We also prepared an N-doped rGO catalyst (denoted as NrGO) following the same synthesis procedure used for  $\text{Mo}_2\text{C-132/NrGO-30}$ , except that no  $\text{Mo}_{132}$  precursors were added. Figure S13 (Supporting Information) shows that NrGO has negligible HER performance, indicating that the excellent HER performance of  $\text{Mo}_2\text{C-132/NrGO-30}$  originates from  $\text{Mo}_2\text{C}$  rather than NrGO. Figure S14a (Supporting Information) illustrates that the four  $\text{Mo}_2\text{C-132/NrGO-}z$  catalysts have similar Tafel slopes of 57–60  $\text{mV dec}^{-1}$ .

**Table 1.** The HER performance of Mo<sub>2</sub>C- $\gamma$ /NrGO-*z* and reference catalysts.

Samples	$\eta_{10}$ [mV]	Tafel slope [mV dec <sup>-1</sup> ]	$C_{dl}$ [mF cm <sup>-2</sup> ]	$j_0$ [mA cm <sup>-2</sup> ]	TOF [s <sup>-1</sup> ]
Mo <sub>2</sub> C-132/NrGO-15	73	59	8.12	0.863	0.68
Mo <sub>2</sub> C-132/NrGO-30	62	57	9.56	1.188	0.70
Mo <sub>2</sub> C-132/NrGO-45	94	59	7.01	0.360	0.35
Mo <sub>2</sub> C-132/NrGO-60	100	60	6.74	0.351	0.30
Mo <sub>2</sub> C-132/rGO-30	102	61	6.18	0.346	0.19
Mo <sub>2</sub> C-36/NrGO-30	143	60	6.03	0.087	0.093
Mo <sub>2</sub> C-12/NrGO-30	152	68	5.43	0.054	0.075
Mo <sub>2</sub> C-7/NrGO-30	185	75	4.27	0.019	–
Pt/C (reference)	47	28	–	1.84	–

Mo<sub>2</sub>C-132/NrGO-30 has the largest exchange current density ( $j_0$ ) of 1.19 mA cm<sup>-2</sup>, which is much higher than that of Mo<sub>2</sub>C-132/NrGO-15 at 0.86 mA cm<sup>-2</sup>, Mo<sub>2</sub>C-132/NrGO-45 at 0.36 mA cm<sup>-2</sup>, and Mo<sub>2</sub>C-132/NrGO-60 at 0.35 mA cm<sup>-2</sup>. Since  $j_0$  reflects the intrinsic electron transfer rate across the electrode/electrolyte interface, the much higher  $j_0$  suggests that Mo<sub>2</sub>C-132/NrGO-30 processes a higher density of catalytically active sites. In addition, Mo<sub>2</sub>C-132/NrGO-30 also has the smallest charge transfer resistance ( $R_{ct}$ ) as determined by electrochemical impedance spectroscopy (EIS) measurement performed at the overpotential of 100 mV (see Figure S14b, Supporting Information). The EIS Nyquist plots of the optimal Mo<sub>2</sub>C-12/NrGO-30 electrocatalyst were collected at different overpotentials (Figure S15, Supporting Information). The  $R_{ct}$  values decrease gradually when higher potentials are applied. Additionally, the Tafel slope calculated by linearly fitting the overpotentials against  $\log(R_{CT}^{-1})$  is 63.5 mV dec<sup>-1</sup>, which is identical to the value determined by Tafel plots.<sup>[14]</sup> We further compared their electrochemical active surface area (ECSA) by determining their double-layer capacitance ( $C_{dl}$ ) via cyclic voltammetry (CV) scans (see Figure S14c, Supporting Information). The results listed in Table 1 show a  $C_{dl}$  for Mo<sub>2</sub>C-132/NrGO-45 of 9.56 mF cm<sup>-2</sup>, which is about  $\approx$ 15, 37, and 42% higher than that of Mo<sub>2</sub>C-132/NrGO-15, -45, and -60, respectively.

We can compare the catalytic activity of Mo<sub>2</sub>C- $\gamma$ /NrGO-*z* electrocatalysts more accurately by calculating their turnover frequencies (TOFs). The calculated TOFs at the  $\eta$  of 100 mV are tabulated in Table 1 (see the details of the calculation in Table S2, Supporting Information). Because of the uniform Mo<sub>2</sub>C nanoparticles and nearly fully exposed active sites on the graphene substrates, Mo<sub>2</sub>C-132/NrGO-15 and Mo<sub>2</sub>C-132/NrGO-30 show similar TOFs of 0.68 and 0.70 s<sup>-1</sup>, respectively (see the inset in Figure 3a). In contrast, the TOFs of Mo<sub>2</sub>C-132/NrGO-45 and Mo<sub>2</sub>C-132/NrGO-60 are much smaller at 0.35 and 0.30 s<sup>-1</sup>, respectively, which can be attributed to the larger Mo<sub>2</sub>C nanoparticle sizes and the formation of Mo<sub>2</sub>C aggregates. If we compare Mo<sub>2</sub>C-132/NrGO-30 with Mo<sub>2</sub>C-132/NrGO-15, although the average size of Mo<sub>2</sub>C nanoparticles in Mo<sub>2</sub>C-132/NrGO-30 increases by  $\approx$ 10% from 2.2 to 2.5 nm, the Mo mass loading in Mo<sub>2</sub>C-132/NrGO-30 is doubled. Thus, it is expected that the density of the catalytic active sites in Mo<sub>2</sub>C-132/NrGO-30 should be much higher than that in Mo<sub>2</sub>C-132/NrGO-15. Considering their similar TOFs, the higher catalytic

active site density may explain the superior HER catalytic performance of Mo<sub>2</sub>C-132/NrGO-30 over Mo<sub>2</sub>C-132/NrGO-15.

We further compare the HER performance of Mo<sub>2</sub>C- $\gamma$ /NrGO catalysts obtained using different Mo precursors. As shown in Figure 3b, Mo<sub>2</sub>C-132/NrGO-30 displays superior HER performance over other Mo<sub>2</sub>C- $\gamma$ /NrGO-30 catalysts. Its  $\eta_{10}$  at 62 mV is much smaller than that of Mo<sub>2</sub>C-36/NrGO-30 at 143 mV, Mo<sub>2</sub>C-12/NrGO-30 at 152 mV, and Mo<sub>2</sub>C-7/NrGO-30 at 185 mV (see Table 1). Tafel slopes and  $j_0$  values listed in Table 1 and Figure 3c show a monotonically decreasing trend with smaller Mo precursors. The  $R_{ct}$  values also have a similar trend. Figure 3d shows that the  $R_{ct}$  values of Mo<sub>2</sub>C-36/NrGO-30, Mo<sub>2</sub>C-12/NrGO-30, and Mo<sub>2</sub>C-7/NrGO-30 increase from 31.2, 39.7 to 47.6  $\Omega$ , which are larger than that of Mo<sub>2</sub>C-132/NrGO-30 at 8.2  $\Omega$ . Figure 3e illustrates that the  $C_{dl}$  values also decrease from 9.56 to 6.03, 5.43, and 4.27 mF cm<sup>-2</sup>, respectively. To obtain a more comprehensive comparison of electrocatalysts prepared using different Mo precursors, we also optimized the mass loading of other Mo precursors (i.e., Mo<sub>7</sub>, Mo<sub>12</sub>, and Mo<sub>36</sub>, see their SEM images and the corresponding EDX mappings in Figures S10–S12, Supporting Information). We observed a clear trade-off in obtaining ultrafine Mo<sub>2</sub>C particles and increasing their mass loading (Figure S16, Supporting Information). Small Mo<sub>2</sub>C particles can only be obtained using these smaller Mo precursors when the Mo mass loadings are significantly reduced (see Table S1, Supporting Information, and TEM images and particle size distributions in Figure S17, Supporting Information). Furthermore, their average sizes are still much larger than that in electrocatalysts derived from Mo<sub>132</sub>. HER performance tested in 0.5 M H<sub>2</sub>SO<sub>4</sub> electrolyte is shown in Figure S17 (Supporting Information). At their optimal mass loadings, the HER performance of electrocatalysts derived from smaller Mo precursors is still inferior to that of the Mo<sub>2</sub>C-132/NrGO-30 electrocatalyst (Figure S18d, Supporting Information). For the Mo<sub>7</sub> and Mo<sub>12</sub> precursors, the poorer HER performance can be partially attributed to their lower Mo mass loadings since relatively small Mo<sub>2</sub>C particles can be obtained. For the Mo<sub>36</sub> precursor, the poorer HER performance is mainly caused by the formation of larger Mo<sub>2</sub>C particles. All these HER performance results indicate the advantage of using the giant Mo<sub>132</sub> precursor in obtaining high-performance Mo<sub>2</sub>C-based catalysts compared to smaller Mo precursors.

The catalytic performance stability of Mo<sub>2</sub>C-132/NrGO-30 was assessed in comparison to commercial 20% Pt/C electrocatalyst. Their discharge curves are shown in Figure 3f. Mo<sub>2</sub>C-132/NrGO-30 can steadily discharge at a large current density of  $-100 \text{ mA cm}^{-2}$  for 24 h. Its required overpotential increases slightly to 24 mV ( $\approx 10.9\%$ ) over the 24 h. In comparison, the overpotential required by the Pt/C catalyst to reach the current density of  $-50 \text{ mA cm}^{-2}$  increases by 247% from 90 to 312 mV in 12 h, showing inferior durability. Furthermore, we have compared the HER performance of Mo<sub>2</sub>C-132/NrGO-30 with other Mo-based HER catalysts published in the literatures (see a detailed comparison in Table S3, Supporting Information), Mo<sub>2</sub>C-132/NrGO-30 shows superior HER performance over most of the cutting-edge Mo<sub>2</sub>C catalysts.<sup>[3b,4,7,8,10c,f,11,12b,15]</sup> To further explore the catalytic activity of Mo<sub>2</sub>C-132/NrGO-30, we also measured the HER performance in 1 M KOH alkaline electrolyte. Figure S19 (Supporting Information) shows that Mo<sub>2</sub>C-132/NrGO-30 exhibits a small  $\eta_{10}$  of 101 mV and a low Tafel slope of  $75 \text{ mV dec}^{-1}$ , which are close to those of the commercial Pt/C electrocatalyst ( $\eta_{10}$  of 73 mV and a Tafel slope of  $57 \text{ mV dec}^{-1}$ ).

In addition to the important role of the Mo<sub>132</sub> precursor, the PEI polymeric binder also plays a critical role in the superior HER activity of the Mo<sub>2</sub>C-132/NrGO catalyst. It would not only serve as a binder, but also nitrogen precursor for N-doping of the graphene nanosheets and carbon precursor for Mo<sub>2</sub>C formation. To further confirm the important role of PEI, two additional electrocatalysts were prepared following the similar synthesis procedure used to prepare the optimal

Mo<sub>2</sub>C-132/NrGO-30, except that one was prepared by adding urea as the N-precursor (denoted as Mo<sub>2</sub>C-132/NrGO-30-U) and the other was prepared without addition of any N precursor (denoted as Mo<sub>2</sub>C-132/rGO-30). The size of Mo<sub>2</sub>C nanoparticles remains relatively small with the average diameter of  $2.6 \pm 0.7$  and  $2.7 \pm 0.8 \text{ nm}$ , respectively (see Figure 4a,b, and Figure S20, Supporting Information), which can be attributed to the giant Mo<sub>132</sub> precursor used. However, the Mo mass loadings in these two electrocatalysts drop significantly to 10.4 and 14.2 wt%, respectively (Figure S21 and Table S1, Supporting Information). The considerably lower Mo mass loadings indicate that the PEI polymeric binder is crucial for anchoring a high mass loading of Mo on the GO surface. We also found the ECSA values decrease to  $7.35 \text{ mF cm}^{-2}$  (Mo<sub>2</sub>C-132/NrGO-30-U) and  $6.18 \text{ mF cm}^{-2}$  (Mo<sub>2</sub>C-132/rGO-30) (Figure S22, Supporting Information) in comparison with  $9.56 \text{ mF cm}^{-2}$  of Mo<sub>2</sub>C-132/NrGO-30. As a result, both Mo<sub>2</sub>C-132/NrGO-30-U and Mo<sub>2</sub>C-132/rGO-30 show inferior HER performance, and their  $\eta_{10}$  values increase to 95 and 102 mV, respectively (Figure 4c).

If we compare Mo<sub>2</sub>C-132/NrGO-30-U and Mo<sub>2</sub>C-132/rGO-30 to Mo<sub>2</sub>C-132/NrGO-15 with a similar Mo mass loading of 12.3 wt%, the TOFs of Mo<sub>2</sub>C-132/NrGO-30-U and Mo<sub>2</sub>C-132/rGO-30 at 0.27 and  $0.19 \text{ s}^{-1}$  are much smaller than that of Mo<sub>2</sub>C-132/NrGO-15 at  $0.68 \text{ s}^{-1}$ . The smaller TOFs imply that PEI plays another role more than just serving as a binder. As we proposed early, PEI can serve as a C source for the formation of Mo<sub>2</sub>C, as well as an N source for doping graphene during the high-temperature annealing process. XPS survey scans show that N atoms have been successfully doped in both

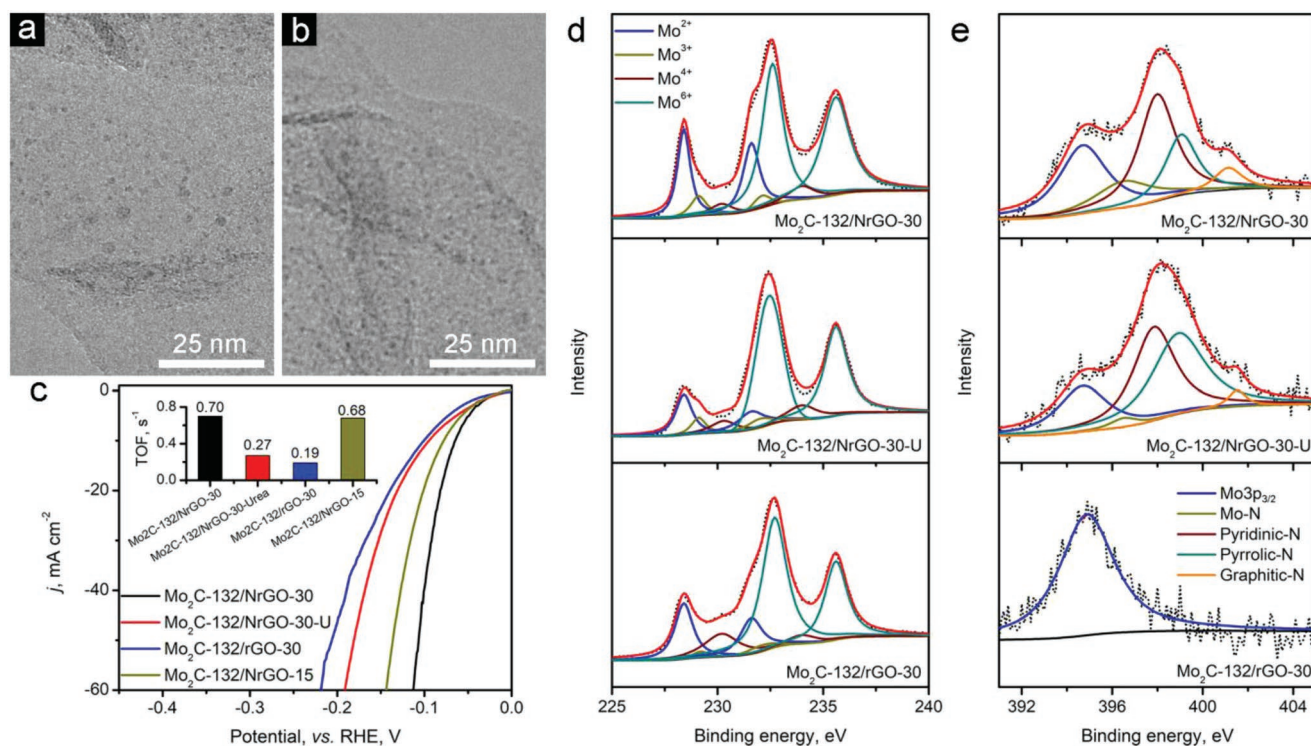


**Figure 4.** a,b) TEM images of Mo<sub>2</sub>C-132/NrGO-30-U and Mo<sub>2</sub>C-132/rGO-30 electrocatalysts. c) LSV curves of various electrocatalysts and their calculated TOFs at  $\eta = 100 \text{ mV}$  (the inset). d,e) High-resolution XPS spectra of Mo 3d and N 1s in Mo<sub>2</sub>C-132/NrGO-30, Mo<sub>2</sub>C-132/NrGO-30-U, and Mo<sub>2</sub>C-132/rGO-30.

Mo<sub>2</sub>C-132/NrGO-30 and Mo<sub>2</sub>C-132/NrGO-30-U at ≈3.99 and 2.26 at% (Figure S23, Supporting Information), respectively. The deconvolution of the high-resolution Mo3d XPS spectra in the three electrocatalysts was performed according to the reported methods,<sup>[4b,8a]</sup> and the results are shown in Figure 4d for comparison. The Mo3d core level XPS spectra split into 3d<sub>5/2</sub> and 3d<sub>3/2</sub> features due to the spin-orbital coupling. The peaks at 228.4 eV (3d<sub>5/2</sub>) and 231.6 eV (3d<sub>3/2</sub>) can be assigned to Mo<sup>2+</sup> in Mo–C, while the peaks at 229.1 and 232.1 eV can be assigned to Mo<sup>3+</sup> in the form of Mo–N interactions. Two pairs of Mo–O peaks can be assigned to Mo<sup>4+</sup> (230.2 and 240.0 eV) and Mo<sup>6+</sup> (232.6 and 235.6 eV) in various Mo oxides due to inevitable oxidative surface contamination during the sample handling.<sup>[5b,16]</sup> It has been proposed that the Mo<sup>3+</sup> features originate from Mo–N interactions.<sup>[17]</sup> The Mo<sup>3+</sup> peak intensity in Mo<sub>2</sub>C-132/NrGO-30 and Mo<sub>2</sub>C-132/NrGO-30-U is much higher than that in Mo<sub>2</sub>C-132/rGO-30, suggesting the formation of Mo–N interactions when PEI or urea was used. To further elaborate the differences among these electrocatalysts, the high-resolution N1s XPS spectra were analyzed (Figure 4e). The peak at 395.7 eV can be assigned to Mo 3p<sub>3/2</sub> features in all three electrocatalysts. Various N features can be assigned to N atoms in pyridinic (398.0 eV), pyrrolic (399.0 eV), and graphitic (401.1 eV) configurations prepared with PEI or urea. No N features were found in Mo<sub>2</sub>C-132/rGO-30. The Mo–N interactions can be identified by the peak at 396.4 eV.<sup>[8b,18]</sup> The intensity of this peak in Mo<sub>2</sub>C-132/NrGO-30-U is much lower than that in Mo<sub>2</sub>C-132/NrGO-30, suggesting that PEI is more efficient in creating Mo–N interactions than urea. Based on these results, we propose that the formation of Mo–N bonds would create a strong interaction between the Mo<sub>2</sub>C nanoclusters and the graphene substrates, which can significantly enhance the HER catalytic activity of the Mo<sub>2</sub>C-based catalysts.

To better understand the mechanism underlying the superior HER activity of Mo<sub>2</sub>C-132/NrGO-30, a series of DFT calculations were performed to study the energy profiles of HER at different potential Mo active sites on graphene or N-doped graphene substrates.<sup>[8a]</sup> Previous calculations have shown that H adsorption is sensitive to the binding sites due to the synergistic effects of ensemble, electronic, and strain.<sup>[19]</sup> Three types of Mo sites in Mo<sub>2</sub>C nanoclusters were considered: the (100) surface Mo, edge Mo, and interface Mo (details of our calculations can be found in the Experimental Section). For each supported Mo<sub>2</sub>C model, three different substrates were considered, including pristine graphene (PG), graphene with graphitic N (GN), and graphene with pyridinic N (PN), which resulted in nine possible Mo sites for investigation (as illustrated in Figure S24, Supporting Information). Structural relaxations show that compared to PG and GN, the substrate with PN has significantly stronger interactions to Mo<sub>2</sub>C, with the interface Mo attracted onto the vacancy (inset in Figure 5a). This calculation is consistent with the observed abundant pyridinic N found in Mo<sub>2</sub>C-132/NrGO-30 (Figure 4d). The calculated free energy profiles of HER at all Mo sites are shown in Figure 5a (the models are illustrated in Figure S25, Supporting Information). The strong binding of H to the (100) and edge Mo sites is close or even stronger than that of pure Mo<sub>2</sub>C(100), leading to comparable HER activity. However, all three types of interface Mo sites have significantly weaker H adsorption. Mo

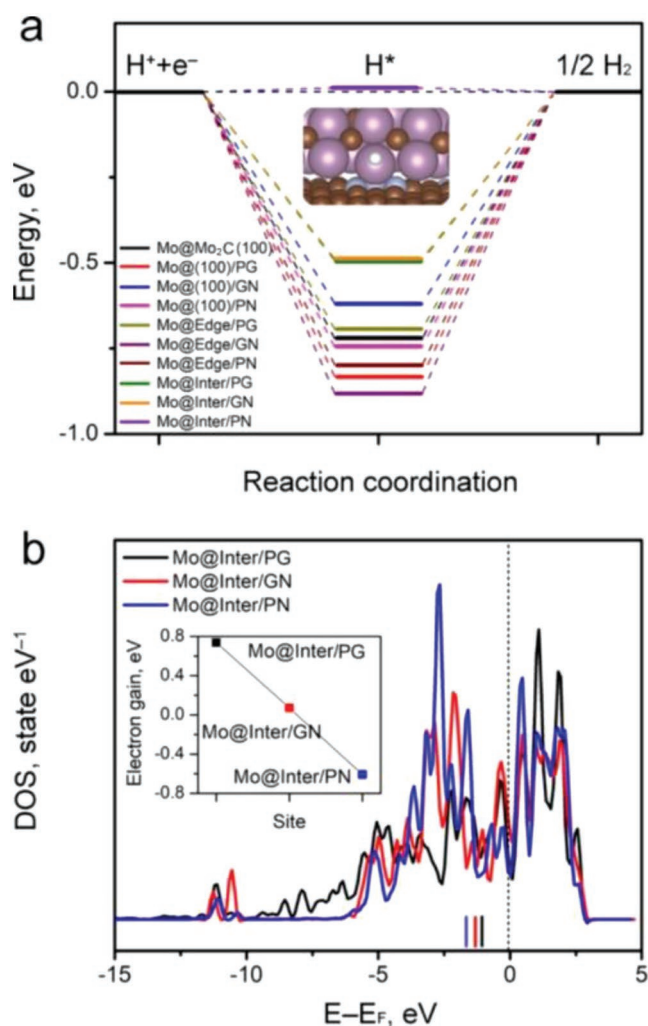


**Figure 5.** a) Calculated free energy profiles of HER at ten different Mo sites. The inset is a schematic illustration of H adsorbed at the interfacial Mo site on the C-pyridinic N (PN) substrate. White, purple, brown, and blue spheres represent H, Mo, C, and N atoms, respectively. b) Calculated PDOS of the interface Mo sites on various substrates. The black vertical dashed line represents the Fermi energy. The colored vertical lines at the bottom indicate the d-band centers. The inset shows the calculated electron gains of each interface Mo site as determined by a Bader charge analysis.

binding at the pyridinic N site has near-zero free energy difference ( $\Delta G = 0.01$  eV), leading to excellent HER activity. This result can also explain the identical TOF values obtained for Mo<sub>2</sub>C-132/NrGO-15 and Mo<sub>2</sub>C-132/NrGO-30. Since the size of Mo<sub>2</sub>C nanoclusters in both electrocatalysts is similar, the number of interfacial active Mo sites should be proportional to their Mo mass loadings, which results in the nearly doubled HER performance, in terms of the current density, for Mo<sub>2</sub>C-132/NrGO-30 as compared to Mo<sub>2</sub>C-132/NrGO-15.

To further understand the significant differences in H<sup>+</sup> binding energies, we calculated the projected density of state (PDOS) of d-electrons of the Mo atoms at the interface supported on the three graphene substrates (Figure 5b). It can be seen from the PDOS that the interfacial Mo atom at the PN site is less contracted than the other two models due to the Mo–N

interactions at the low-energy region. The calculated d-band centers of the three Mo sites (colored lines in Figure 5b) show that the interfacial Mo atom at the PN site is the furthest from the Fermi level, which correlates well with their H adsorption trends. The calculated electron gains of these three interfacial Mo (inset in Figure 5b) further confirm that the stronger Mo–N interaction in the PN sites results in electron loss from Mo and a weakened hydrogen binding, which leads to the high HER activity.

In summary, we have shown that a giant POM (Mo<sub>132</sub>) can yield Mo<sub>2</sub>C catalysts with near-uniform nanoparticles with a size of 2.5 ± 0.7 nm and an ultrahigh mass loading up to 27.5 wt%. Control of these Mo<sub>2</sub>C nanoparticles has been achieved by using Mo<sub>132</sub> instead of small counterparts. Besides, PEI is found to be a suitable polymeric binder for assisting the uniform distribution of Mo<sub>132</sub> on graphene surface. On top, serving as a N source, PEI also favors the formation of strong Mo–N bonds, which suppress the aggregation of Mo<sub>2</sub>C nanoparticles during high-temperature annealing. Combining experimental (XPS analysis) and computational (DFT calculations) results, it is found that the strong Mo–N interactions created between Mo<sub>2</sub>C nanoparticles and N-doped graphene substrates significantly enhances the HER activity. The optimal Mo<sub>2</sub>C-132/NrGO-30 catalyst requires 62 mV to deliver a current density of 10 mA cm<sup>-2</sup>, a large  $j_0$  of 1.19 mA cm<sup>-2</sup>, a high TOF of 0.70 s<sup>-1</sup> (at  $\eta = 100$  mV), as well as excellent durability, which surpasses most of the cutting-edge Mo<sub>2</sub>C catalysts reported so far. The design principles demonstrated in this work is useful as a general strategy for discovering high-performing catalysts based on uniform metal carbide nanoparticles.

## Experimental Section

**Material Synthesis:** The polyoxomolybdate clusters were synthesized following methods described earlier.<sup>[12a,c]</sup> Chemicals used were obtained from Sigma-Aldrich without further treatment. Briefly, the (NH<sub>4</sub>)<sub>42</sub>[Mo<sub>132</sub>O<sub>372</sub>(CH<sub>3</sub>COO)<sub>30</sub>(H<sub>2</sub>O)<sub>72</sub>]·10CH<sub>3</sub>COONH<sub>4</sub>·300H<sub>2</sub>O (Mo<sub>132</sub>) cluster was prepared by first dissolving 5.6 g (NH<sub>4</sub>)<sub>6</sub>Mo<sub>7</sub>O<sub>24</sub>·4H<sub>2</sub>O (99.98%) and 12.5 g CH<sub>3</sub>COONH<sub>4</sub> (≥98%) in 250 mL deionized water (DI-H<sub>2</sub>O). Then, 0.8 g N<sub>2</sub>H<sub>4</sub>·H<sub>2</sub>SO<sub>4</sub> (≥99%) was added. The mixture was stirred for several minutes until it changed to blue-green in color. Afterward, 83 mL of 50 vol% CH<sub>3</sub>COOH (≥99%) was added. The mixture was allowed to precipitate for 4 d. Red-brown crystals were obtained by filtration and then washed with 90% ethanol and diethyl ether. Mo<sub>36</sub> clusters were synthesized by mixing equal volumes of 0.2 M K<sub>2</sub>MoO<sub>4</sub> and 0.4 M HNO<sub>3</sub> solution at room temperature. After 6 d of precipitation, colorless, transparent columnar crystals of Mo<sub>36</sub> were obtained by filtration. Mo<sub>7</sub> and Mo<sub>12</sub> were purchased from Sigma-Aldrich.

Other Mo<sub>2</sub>C- $\gamma$ /NrGO- $z$  catalysts were prepared following the same method. Generally, 10 mL GO solution (4 mg mL<sup>-1</sup>, prepared by a modified Hummers method<sup>[20]</sup>) was first mixed with 10 mL PEI solution (2 mg mL<sup>-1</sup>, prepared by diluting 50% branched PEI solution (w/v in DI-H<sub>2</sub>O)) by stirring for 15 min. Afterward, 20 mL of Mo<sub>132</sub> solutions containing different amount of Mo<sub>132</sub> clusters (16, 38, 77, or 136 mg corresponding to 15, 30, 45, and 60 wt% of Mo) were added to the mixture under stirring. The Mo loadings were designed based on the mass fraction of Mo in the total mass of Mo and GO (40 mg) used because other elements would most likely decompose during the high-temperature annealing. For example, 38 mg of the Mo<sub>132</sub> precursors (containing 38 × 44% = 16.72 mg of Mo) were added to 40 mg of GO, resulting in the designed Mo mass loading of 30 wt% (16.72/(16.72 + 40) = 30 wt%). The mixture was then further

homogenized by tip sonication for 10 min in ice-water bath (VCX-130, Sonics). Next, the resulting mixture (40 mL) was subjected to hydrothermal reaction at 180 °C for 12 h in Teflon-lined stainless-steel autoclave. The solid products were recovered by filtration, washed with DI water, and then freeze-dried at –80 °C. A three-step annealing process was used to prepare the electrocatalysts. The freeze-dried materials were first heated to 300 °C at a ramping rate of 5 °C min<sup>-1</sup> and annealed at 300 °C for 15 min under air. Next, the materials were reduced under a H<sub>2</sub> flow rate of 100 sccm at 300 °C for 30 min. Finally, the reduced materials were heated to 850 °C at the temperature ramping rate of 10 °C min<sup>-1</sup> and annealed for 2 h under 200 sccm Ar flow. The resulting catalysts were denoted as Mo<sub>2</sub>C-132/NrGO- $z$  ( $z$  corresponds to the mass loading of Mo at 15, 30, 45, and 60 wt%). Mo<sub>2</sub>C- $\gamma$ /NrGO-30 ( $\gamma$  corresponds to the number of Mo atoms in Mo precursors) catalysts were prepared following the same procedure used for Mo<sub>2</sub>C-132/NrGO-30, except that Mo<sub>132</sub> clusters were replaced with 32.6 mg of Mo<sub>36</sub> clusters, 28 mg of Mo<sub>12</sub>, or 31.5 mg of Mo<sub>7</sub> as precursors. These catalysts contain about 30 wt% Mo.

**Material Characterization:** FTIR (KBr pellet, Thermo-Fisher Nicolet) was applied to characterize synthesized Mo<sub>132</sub> and Mo<sub>36</sub> clusters. SEM and EDS were performed on a Zeiss Ultra-Plus microscope. TEM was carried out on a JEOL JEM-2100F microscope. HAADF-STEM was performed on a FEI Themis-Z microscope. XRD patterns were recorded at room temperature using a Shimadzu XRD-6000 diffractometer. XPS were collected on a VG Escalab210 instrument with an Al source. The elemental composition was analyzed by EDX and ICP-AES (Agilent Varian). The surface area and pore size distribution were calculated from N<sub>2</sub> adsorption–desorption isotherms collected on an Autosorb iQ-C gas adsorption instrument.

**Electrode Preparation:** The electrocatalyst ink was prepared by dispersing 5 mg of each type of electrocatalysts in 1 mL of water/isopropanol solution (1:9 v/v) together with 0.05 wt% Nafion 117 by bath ultrasonication. The electrodes were fabricated by drop casting 2.9  $\mu$ L of the electrocatalyst ink on prepolished GCEs with the geometric area of 0.07 cm<sup>2</sup>. The mass loading density of electrocatalyst on each GCE is about 0.2 mg cm<sup>-2</sup>. The electrodes were dried overnight before electrochemical performance tests. Commercial Pt/C electrocatalysts (20 wt% Pt on Vulcan XC-72) were used to fabricate reference electrodes with the same electrocatalyst mass loading density on GCEs.

**Electrochemical Tests:** HER electrocatalytic performance of fabricated electrodes was tested on an electrochemical workstation (CHI 660E) in a three-electrode configuration. All reported potentials were calibrated to a RHE. A SCE and a carbon rod (99.999%, BASi) were used as the reference and the counter electrode, respectively. The electrolyte was saturated with H<sub>2</sub> (Coregas, 99.999%). CV curves were collected at a scan rate of 50 mV s<sup>-1</sup>. LSV polarization curves were recorded at a scan rate of 2 mV s<sup>-1</sup> with 95%  $iR$  compensation, and Tafel analysis was recorded at the same scan rate. Tafel slope was recorded at the same scan rate and the results were fitted by  $\eta = a + b \log(j)$ , where  $\eta$  is the overpotential (in mV),  $j$  is the current density (in mA cm<sup>-2</sup>). The fitted constant of  $b$  is the Tafel slope and  $a$  is used to calculate the exchange current density  $j_0$ . EIS data were recorded at –0.1 V versus RHE in the frequency range from 0.1 to 10<sup>5</sup> Hz. ECSA was estimated by the surface double-layer capacitances ( $C_{dl}$ ) of various electrocatalysts, which were determined by linearly fitting of the ( $j_{anodic} - j_{cathodic}$ )/2 values obtained from CV scans performed at different scan rates in a non-Faradaic region. All the electrochemical tests were repeated on at least three different electrodes for every electrocatalyst.

**Computational Methods:** All DFT calculations were performed using the VASP code. Electron correlation was considered using the generalized gradient approximation (GGA) method and the Perdew–Burke–Ernzerhof (PBE) functional,<sup>[21]</sup> while core electrons were considered with the projector augmented wave (PAW) method.<sup>[22]</sup> Kohn–Sham wave functions were expanded in a plane wave basis set for the valence electrons.<sup>[23]</sup> The Brillouin zone was sampled using a (3 × 3 × 1) Monkhorst–Pack  $k$ -point mesh and integrated with the Methfessel and Paxton method.<sup>[24]</sup> A vacuum gap of at least 12 Å was used to separate periodic images between supercells. Geometries were considered

converged when all the forces of each atom fell below 0.05 eV. Spin polarization was tested and performed when necessary. The electron charge transfer was performed using a Bader charge analysis.<sup>[25]</sup> The free energy of HER  $\Delta G_{H^*}$  at different Mo sites was calculated using Equation (1)

$$\Delta G_{H^*} = \Delta E_{H^*} + 0.24 \text{ eV} \quad (1)$$

where  $\Delta E_{H^*}$  is the hydrogen binding energy with a gas phase hydrogen molecule as the energy reference, and 0.24 eV is an entropic and zero point energy correction.<sup>[26]</sup>

To model the Mo<sub>2</sub>C electrocatalysts synthesized in this study, their structure was modeled as a double-layer Mo<sub>2</sub>C nanorod with a (100) surface in the z-direction supported on a (6 × 6) graphene cell. This system contains three Mo sites: (100), edge, and interface, representing Mo atoms in different coordination environments. To evaluate the effect of N-doping in graphene, both nondefected and defected situations were considered. The nondefected graphene was modeled as a C-graphitic N (GN) substrate, while the defected graphene was modeled as a C-pyridinic N (PN) substrate (Figure S23, Supporting Information) according to previous theoretical studies.<sup>[15c]</sup> The top, side, and bottom views of these models can be found in Figure S25 (Supporting Information). A (4 × 4) double-layer (100) Mo<sub>2</sub>C without graphene was also modeled for further additional comparison.

## Supporting Information

Supporting Information is available from the Wiley Online Library or from the author.

## Acknowledgements

The authors thank funding support from Australian Research Council under the Future Fellowships scheme (FT160100107), Discovery Programme (DP180102210), and the Faculty of Engineering, Information and Technology of The University of Sydney under the Early Career Researcher Scheme. The computational work was supported by the Welch Foundation (F-1841) and the Texas Advanced Computing Center. The authors thank Hongru Ding for providing graphics of Mo clusters.

## Conflict of Interest

The authors declare no conflict of interest.

## Keywords

graphene, hydrogen evolution reaction, molybdenum carbide, polyoxomolybdate

Received: January 18, 2019  
Published online:

- [1] a) S. Chu, Y. Cui, N. Liu, *Nat. Mater.* **2017**, *16*, 16; b) P. C. K. Vesborg, B. Seger, I. Chorkendorff, *J. Phys. Chem. Lett.* **2015**, *6*, 951; c) S. Ardo, D. F. Rivas, M. A. Modestino, V. S. Greiving, F. F. Abdi, E. A. Llado, V. Artero, K. Ayers, C. Battaglia, J.-P. Becker, D. Bederak, A. Berger, F. Buda, E. Chinello, B. Dam, V. Di Palma, T. Edvinsson, K. Fujii, H. Gardeniers, H. Geerlings, S. M. H. Hashemi, S. Haussener, F. Houle, J. Huskens, B. D. James, K. Konrad, A. Kudo, P. P. Kunturu, D. Lohse, B. Mei, E. L. Miller, G. F. Moore, J. Muller, K. L. Orchard, T. E. Rosser, F. H. Saadi, J.-W. Schüttauf,

- B. Seger, S. W. Sheehan, W. A. Smith, J. Spurgeon, M. H. Tang, R. van de Krol, P. C. K. Vesborg, P. Westerik, *Energy Environ. Sci.* **2018**, *11*, 2768; d) Z. W. Seh, J. Kibsgaard, C. F. Dickens, I. Chorkendorff, J. K. Nørskov, T. F. Jaramillo, *Science* **2017**, *355*, eaad4998.
- [2] a) S. Anantharaj, S. R. Ede, K. Sakthikumar, K. Karthick, S. Mishra, S. Kundu, *ACS Catal.* **2016**, *6*, 8069; b) V. Vij, S. Sultan, A. M. Harzandi, A. Meena, J. N. Tiwari, W.-G. Lee, T. Yoon, K. S. Kim, *ACS Catal.* **2017**, *7*, 7196; c) L. Zhang, J. Xiao, H. Wang, M. Shao, *ACS Catal.* **2017**, *7*, 7855; d) Y. Zheng, Y. Jiao, A. Vasileff, S. Z. Qiao, *Angew. Chem., Int. Ed.* **2018**, *57*, 7568.
- [3] a) M. Miao, J. Pan, T. He, Y. Yan, B. Y. Xia, X. Wang, *Chem. - Eur. J.* **2017**, *23*, 10947; b) Y. Liu, G. Yu, G.-D. Li, Y. Sun, T. Asefa, W. Chen, X. Zou, *Angew. Chem., Int. Ed.* **2015**, *54*, 10752; c) W. F. Chen, C. H. Wang, K. Sasaki, N. Marinkovic, W. Xu, J. T. Muckerman, Y. Zhu, R. R. Adzic, *Energy Environ. Sci.* **2013**, *6*, 943; d) W.-F. Chen, J. T. Muckerman, E. Fujita, *Chem. Commun.* **2013**, *49*, 8896.
- [4] a) C. B. Lu, D. Tranca, J. Zhang, F. R. Hernandez, Y. Z. Su, X. D. Zhuang, F. Zhang, G. Seifert, X. L. Feng, *ACS Nano* **2017**, *11*, 3933; b) R. Ma, Y. Zhou, Y. Chen, P. Li, Q. Liu, J. Wang, *Angew. Chem., Int. Ed.* **2015**, *54*, 14723.
- [5] a) H. Vruble, X. Hu, *Angew. Chem., Int. Ed.* **2012**, *51*, 12703; b) C. Wan, Y. N. Regmi, B. M. Leonard, *Angew. Chem., Int. Ed.* **2014**, *53*, 6407.
- [6] a) F. Li, X. Zhao, J. Mahmood, M. S. Okyay, S. M. Jung, I. Ahmad, S. J. Kim, G. F. Han, N. Park, J. B. Baek, *ACS Nano* **2017**, *11*, 7527; b) D. H. Youn, S. Han, J. Y. Kim, J. Y. Kim, H. Park, S. H. Choi, J. S. Lee, *ACS Nano* **2014**, *8*, 5164; c) Y. Y. Chen, Y. Zhang, W. J. Jiang, X. Zhang, Z. Dai, L. J. Wan, J. S. Hu, *ACS Nano* **2016**, *10*, 8851; d) J. Dong, Q. Wu, C. Huang, W. Yao, Q. Xu, *J. Mater. Chem. A* **2018**, *6*, 10028.
- [7] a) F. X. Ma, H. B. Wu, B. Y. Xia, C. Y. Xu, X. W. Lou, *Angew. Chem., Int. Ed.* **2015**, *54*, 15395; b) H. B. Wu, B. Y. Xia, L. Yu, X. Y. Yu, X. W. Lou, *Nat. Commun.* **2015**, *6*, 6512.
- [8] a) Y. Huang, Q. Gong, X. Song, K. Feng, K. Nie, F. Zhao, Y. Wang, M. Zeng, J. Zhong, Y. Li, *ACS Nano* **2016**, *10*, 11337; b) H. Yan, Y. Xie, Y. Jiao, A. Wu, C. Tian, X. Zhang, L. Wang, H. Fu, *Adv. Mater.* **2018**, *30*, 1704156; c) Y. P. Zhu, G. Chen, X. M. Xu, G. M. Yang, M. L. Liu, Z. P. Shao, *ACS Catal.* **2017**, *7*, 3540; d) H. Lin, N. Liu, Z. Shi, Y. Guo, Y. Tang, Q. Gao, *Adv. Funct. Mater.* **2016**, *26*, 5590; e) C. Tang, W. Wang, A. Sun, C. Qi, D. Zhang, Z. Wu, D. Wang, *ACS Catal.* **2015**, *5*, 6956.
- [9] a) Q. Cao, S. J. Han, J. Tersoff, A. D. Franklin, Y. Zhu, Z. Zhang, G. S. Tulevski, J. S. Tang, W. Haensch, *Science* **2015**, *350*, 68; b) L. F. Fei, S. M. Ng, W. Lu, M. Xu, L. L. Shu, W. B. Zhang, Z. H. Yong, T. Y. Sun, C. H. Lam, C. W. Leung, C. L. Mak, Y. Wang, *Nano Lett.* **2016**, *16*, 7875.
- [10] a) Z.-Y. Yu, Y. Duan, M.-R. Gao, C.-C. Lang, Y.-R. Zheng, S.-H. Yu, *Chem. Sci.* **2017**, *8*, 968; b) Z. Cheng, J. Gao, Q. Fu, C. Li, X. Wang, Y. Xiao, Y. Zhao, Z. Zhang, L. Qu, *ACS Appl. Mater. Interfaces* **2017**, *9*, 24608; c) L. Chen, H. Jiang, H. Jiang, H. Zhang, S. Guo, Y. Hu, C. Li, *Adv. Energy Mater.* **2017**, *7*, 1602782; d) Y. Jin, H. Wang, J. Li, X. Yue, Y. Han, P. K. Shen, Y. Cui, *Adv. Mater.* **2016**, *28*, 3785; e) L. F. Pan, Y. H. Li, S. Yang, P. F. Liu, M. Q. Yu, H. G. Yang, *Chem. Commun.* **2014**, *50*, 13135; f) Z. Shi, K. Nie, Z.-J. Shao, B. Gao, H. Lin, H. Zhang, B. Liu, Y. Wang, Y. Zhang, X. Sun, X.-M. Cao, P. Hu, Q. Gao, Y. Tang, *Energy Environ. Sci.* **2017**, *10*, 1262; g) S. Wang, J. Wang, M. Zhu, X. Bao, B. Xiao, D. Su, H. Li, Y. Wang, *J. Am. Chem. Soc.* **2015**, *137*, 15753; h) Y. Zhao, K. Kamiya, K. Hashimoto, S. Nakanishi, *J. Am. Chem. Soc.* **2015**, *137*, 110.
- [11] Y. Huang, J. Ge, J. Hu, J. Zhang, J. Hao, Y. Wei, *Adv. Energy Mater.* **2017**, 1701601.
- [12] a) B. Krebs, I. Paulat-Boschen, *Acta Crystallogr., Sect. B: Struct. Crystallogr. Cryst. Chem.* **1982**, *38*, 1710; b) H. W. Liang, S. Bruller, R. Dong, J. Zhang, X. Feng, K. Mullen, *Nat. Commun.* **2015**, *6*, 7992;

- c) A. Muller, E. Krickemeyer, H. Bogge, M. Schmidtman, F. Peters, *Angew. Chem., Int. Ed.* **1998**, *37*, 3360.
- [13] A. Chychko, L. Teng, S. Seetharaman, *Steel Res. Int.* **2010**, *81*, 784.
- [14] H. Vrubel, T. Moehl, M. Grätzel, X. Hu, *Chem. Commun.* **2013**, *49*, 8985.
- [15] a) M. A. R. Anjum, J. S. Lee, *ACS Catal.* **2017**, *7*, 3030; b) H. Fei, J. Dong, M. J. Arellano-Jimenez, G. Ye, N. Dong Kim, E. L. Samuel, Z. Peng, Z. Zhu, F. Qin, J. Bao, M. J. Yacaman, P. M. Ajayan, D. Chen, J. M. Tour, *Nat. Commun.* **2015**, *6*, 8668; c) J. S. Li, Y. Wang, C. H. Liu, S. L. Li, Y. G. Wang, L. Z. Dong, Z. H. Dai, Y. F. Li, Y. Q. Lan, *Nat. Commun.* **2016**, *7*, 11204; d) L. Ma, L. R. L. Ting, V. Molinari, C. Giordano, B. S. Yeo, *J. Mater. Chem. A* **2015**, *3*, 8361; e) E. J. Popczun, C. G. Read, C. W. Roske, N. S. Lewis, R. E. Schaak, *Angew. Chem., Int. Ed.* **2014**, *53*, 5427; f) Z. H. Zhao, F. Qin, S. Kasiraju, L. X. Xie, M. K. Alam, S. Chen, D. Z. Wang, Z. F. Ren, Z. M. Wang, L. C. Grabow, J. M. Bao, *ACS Catal.* **2017**, *7*, 7312.
- [16] K. Oshikawa, M. Nagai, S. Omi, *J. Phys. Chem. B* **2001**, *105*, 9124.
- [17] Z. B. Wei, P. Grange, B. Delmon, *Appl. Surf. Sci.* **1998**, *135*, 107.
- [18] S. Gong, Z. Jjiang, P. Shi, J. Fan, Q. Xu, Y. Min, *Appl. Catal., B* **2018**, *238*, 318.
- [19] a) H. Li, G. Henkelman, *J. Phys. Chem. C* **2017**, *121*, 27504; b) G. W. Piburn, H. Li, P. Kunal, G. Henkelman, S. M. Humphrey, *ChemCatChem* **2018**, *10*, 329; c) L. Luo, Z. Y. Duan, H. Li, J. Kim, G. Henkelman, R. M. Crooks, *J. Am. Chem. Soc.* **2017**, *139*, 5538; d) P. Kunal, H. Li, B. L. Dewing, L. Zhang, K. Jarvis, G. Henkelman, S. M. Humphrey, *ACS Catal.* **2016**, *6*, 4882; e) H. Li, L. Luo, P. Kunal, C. S. Bonifacio, Z. Y. Duan, J. C. Yang, S. M. Humphrey, R. M. Crooks, G. Henkelman, *J. Phys. Chem. C* **2018**, *122*, 2712; f) E. J. Evans, H. Li, W. Y. Yu, G. M. Mullen, G. Henkelman, C. B. Mullins, *Phys. Chem. Chem. Phys.* **2017**, *19*, 30578.
- [20] D. C. Marcano, D. V. Kosynkin, J. M. Berlin, A. Sinitskii, Z. Z. Sun, A. Slesarev, L. B. Alemany, W. Lu, J. M. Tour, *ACS Nano* **2010**, *4*, 4806.
- [21] a) J. P. Perdew, K. Burke, M. Ernzerhof, *Phys. Rev. Lett.* **1996**, *77*, 3865; b) G. Kresse, J. Furthmuller, *Phys. Rev. B* **1996**, *54*, 11169.
- [22] P. E. Blochl, *Phys. Rev. B* **1994**, *50*, 17953.
- [23] W. Kohn, L. J. Sham, *Phys. Rev.* **1965**, *140*, A1133.
- [24] H. J. Monkhorst, J. D. Pack, *Phys. Rev. B* **1976**, *13*, 5188.
- [25] W. Tang, E. Sanville, G. Henkelman, *J. Phys.: Condens. Matter* **2009**, *21*, 084204.
- [26] L. Zhang, G. Henkelman, *ACS Catal.* **2015**, *5*, 655.